Title

Why superconducting Ta qubits have fewer tunneling two-level systems at the vacuum-oxide interface than Nb qubits

Journal

Physical Review Applied, 23(2)

ISSN

2331-7043

Authors

Wang, Zhe

Yu, Clare C

Wu, Ruqian

Publication Date

2025-02-01

DOI

10.1103/physrevapplied.23.024017

Why superconducting Ta qubits have fewer tunneling two-level systems at the vacuum-oxide interface than Nb qubits

Zhe Wang, Clare C. Yu, and Ruqian Wu*
Department of Physics and Astronomy, University of California, Irvine, CA 92697, USA

(Received 8 April 2024; revised 10 January 2025; accepted 13 January 2025; published 6 February 2025)

Superconducting qubits are a key contender for quantum computing elements, but they often face challenges like noise and decoherence from two-level systems (TLSs). Tantalum (Ta) qubits are notable for their long T_1 coherence times, nearing milliseconds, presumably due to fewer TLSs, though the cause of this is unclear. We explore this by analyzing the vacuum-oxide interface using density functional theory, particularly comparing Nb oxide (Nb_2O_5) and Ta oxide (Ta_2O_5). We discover that Ta_2O_5 forms a smoother surface with fewer dangling O atoms and structural TLSs than Nb_2O_5. The greater atomic mass of Ta also lowers the tunnel splittings of these structural TLSs below the qubit's operating frequency. Furthermore, using external electric fields or SO_2 passivation can significantly reduce defect-related TLSs on Nb surfaces, potentially improving their coherence times.

DOI: 10.1103/PhysRevApplied.23.024017

I. INTRODUCTION

Superconducting qubits, which are widely regarded as a leading technology for scalable quantum computing, have seen substantial progress [1,2]. Over the past two decades, their T_1 coherence times have dramatically improved, extending from less than 1 ns to hundreds of μs [3,4]. Further development of superconducting qubits with much longer coherence times is crucial for the realization of large-scale fault-tolerant quantum computers. A significant obstacle to this enhancement is the presence of two-level systems (TLSs) [5–8], which can arise from various mechanisms: atom [9–11] or electron [12] tunneling between the minima of a double-well potential, nearly degenerate spin states [13], trapping and release of quasiparticles [14], or the electronic energy levels of an impurity atom [15]. If the tunneling entity between two potential minima is charged, such as in the case of the structural TLS discussed in this work, its electric dipole moment can couple to both the qubit and microwaves in quantum circuits, leading to dielectric loss [5], charge noise [16], and critical current noise [17]. When the TLS energy splitting matches the qubit energy, the qubit can resonantly transfer its excitation energy to the TLS, leading to a significant reduction in the qubit's relaxation time T_1 [5,6].

Structural TLSs are predominantly found in the native oxide layers on the surface of superconducting qubits; however, the microscopic nature of these TLSs remains elusive, even in conventional qubit materials like aluminum (Al) and niobium (Nb) [4,18–22]. The T_1 relaxation time of Al qubits is limited to about 70 μs [23], and that of Nb qubits is about 60 μs [19,24], indicating a significant density of defect-induced TLSs in these materials. Recent studies have identified tantalum (Ta) as a particularly promising qubit material for quantum computing [25,26]. In 2021, Place *et al.* [25] found that Ta transmon qubits deposited on sapphire had remarkably long coherence times, surpassing 0.3 ms [25] and later reaching an impressive 0.5 ms [26]. The reasons for these enhanced performance metrics in Ta-based devices have not yet been elucidated. As Ta and Nb share similar properties, the difference in their performance in quantum applications is striking. This difference may only be partially attributed to variations in the composition at the metal-oxide interface [19,25]. Specifically, while Nb is prone to forming multiple suboxides such as NbO and NbO_2 between the Nb metal and the outermost Nb_2O_5 layers [18–21,27], Ta consistently forms a highly homogeneous Ta_2O_5 layer [26], as also verified by our phase-diagram calculations (see Appendix A).

Recently, vacuum-oxide interfaces have been identified as more significant sources of structural TLSs on Al qubits [28,29]. These findings prompted us to explore the puzzling differences between the vacuum-oxide interfaces of Nb and Ta, despite their outermost oxide layers, Nb_2O_5 and Ta_2O_5, sharing similar chemical compositions and properties. Studying the differences in the formation of structural TLSs between Nb and Ta is essential for optimizing material selection and surface treatments for superconducting devices such as qubits. Specifically, exploring their structural and electronic subtleties is crucial, given

*Contact author: wur@uci.edu

the high sensitivity of the energy levels of structural TLSs to local conditions.

In this work, we explore the potential for structural TLSs to reside on Nb_2O_5 and Ta_2O_5 surfaces through density functional theory (DFT) calculations. Our findings reveal that the energetically favored Nb_2O_5 surfaces are rough with dangling O atoms, which form detrimental TLSs with tunnel splittings in the GHz range. In contrast, Ta_2O_5 tends to form smoother surfaces with fewer dangling O atoms. Moreover, the greater atomic mass of Ta shifts the frequencies of TLSs below the GHz range. These findings offer a new explanation for the unexpectedly long coherence times recently observed in Ta-based qubits [25,26], distinct from the previous suggestion that attributed the effect to suboxide formation in Nb films. We also demonstrate that the energy splittings of these structural TLSs can be effectively pushed away from the operating frequencies of qubits by applying a small dc electric field. In addition, the density of structural TLSs can be reduced by passivating the surface with sulfur dioxide (SO_2) gas. These insights could contribute to further extending the coherence times of superconducting qubits.

II. COMPUTATIONAL METHODS

Our DFT calculations were performed using the projector augmented-wave (PAW) [30] method as implemented in the Vienna *ab initio* simulation package (VASP) [31,32]. The exchange-correlation functional was described by the generalized gradient approximation (GGA), in the form proposed by Perdew, Burke, and Ernzerhof (PBE) [33,34]. An energy cutoff of 550 eV was used for the plane-wave basis expansion. In the bulk calculations, a Γ-centered Monkhorst-Pack k-point mesh of $2 \times 5 \times 4$ was adopted for the Brillouin-zone integration, and both the lattice constants and atomic positions were fully relaxed until the force acting on each atom was less than 0.01 eV/Å. In the subsequent slab calculations, the in-plane lattice constants were fixed at their bulk values. When exploring the TLSs formed by dangling O atoms, the climbing image nudged elastic band (CI-NEB) [35] method was used to determine the barrier height of the double-well potential. It has been reported that the PBE functional without van der Waals (vdW) corrections predicts incorrect ground-state phases for Nb_2O_5 and Ta_2O_5. We therefore included the vdW correction using the DFT-D3 [36] method with the Becke-Johnson damping function [37] in all of the calculations. Structure visualization was performed using the VESTA [38] package.

Although our main conclusions were obtained using the crystalline phase of Nb_2O_5, they are also applicable to real amorphous surface oxides. This is because TLSs are determined by local atomic environments rather than by long-range order. To further demonstrate this, we generated amorphous surfaces using molecular dynamics (MD) simulations with machine-learning force fields (MLFFs) [39–41]. This approach allows us to simulate large system sizes and time scales while maintaining near *ab initio* accuracy. We performed melt-and-quench MD runs, a common method for generating amorphous structures [42–45]. The NVT ensemble with a Langevin thermostat was used, because an NPT ensemble would automatically drive the surface to bulk structures during long MD runs; however, the surface system can still eventually reach the densities of amorphous structures, as the atoms are free to expand along the z direction.

The on-the-fly MLFFs were trained using a small supercell of the B-M_2O_5(010) (M = Nb or Ta) surface with lattice constants greater than 10 Å. During training, we first melted the Nb_2O_5 surface at 2400 K ($T_{melt} = 1785$ K) and the Ta_2O_5 surface at 2700 K ($T_{melt} = 2145$ K) for 30 ps. We then quenched the system to 300 K with a cooling rate of 30 K/ps, which is the same order of magnitude as that used in previous works [43–45]. After that, the structure was equilibrated at 300 K for 30 ps and subsequently cooled to 0 K in 30 ps.

Based on the generated MLFFs, we repeated the melt-and-quench processes using a much larger supercell, with lattice constants greater than 100 Å (8064 atoms). To ensure our conclusions were independent of the cooling rate, we carried out MD runs with varying cooling rates of 240, 120, 60, 30, 15, and 7.5 K/ps. We also tested training and running from different surface orientations and found that our conclusions remained mostly unchanged.

III. RESULTS AND DISCUSSIONS

The oxides that form on metal surfaces are generally amorphous, meaning that they are challenging to model in DFT calculations. Here, we use crystalline structures with large supercells [9,10,13,46,47] to mimic the local atomic environments that give rise to structural TLS and, furthermore, demonstrate that our conclusions are applicable to amorphous surfaces through MD simulations. For the crystalline structures, we adopt the most prominent B-phase of Nb_2O_5 [48] and Ta_2O_5 [49] (space group $C2/c$; for detailed discussions about its energetic stability, see Appendix B). As illustrated in Fig. 1(a), the B-M_2O_5 structure (M = Nb, Ta) features pairs of MO_6 octahedra, with adjacent pairs linked through corner-sharing. The optimized lattice parameters for the bulk B-Nb_2O_5 and B-Ta_2O_5, as listed in Table I of Appendix B, deviate by less than 0.9% from the experimental values. We begin by exploring the preferential orientation and termination of the vacuum-oxide interfaces of B-Nb_2O_5 and B-Ta_2O_5. We consider their (100), (010), and (001) surfaces with all possible terminations, either stoichiometric (see Appendix C) or nonstoichiometric. Their surface energies dictate that the most preferable configurations are all stoichiometric, denoted as (100), (010)-III, and (001)-II

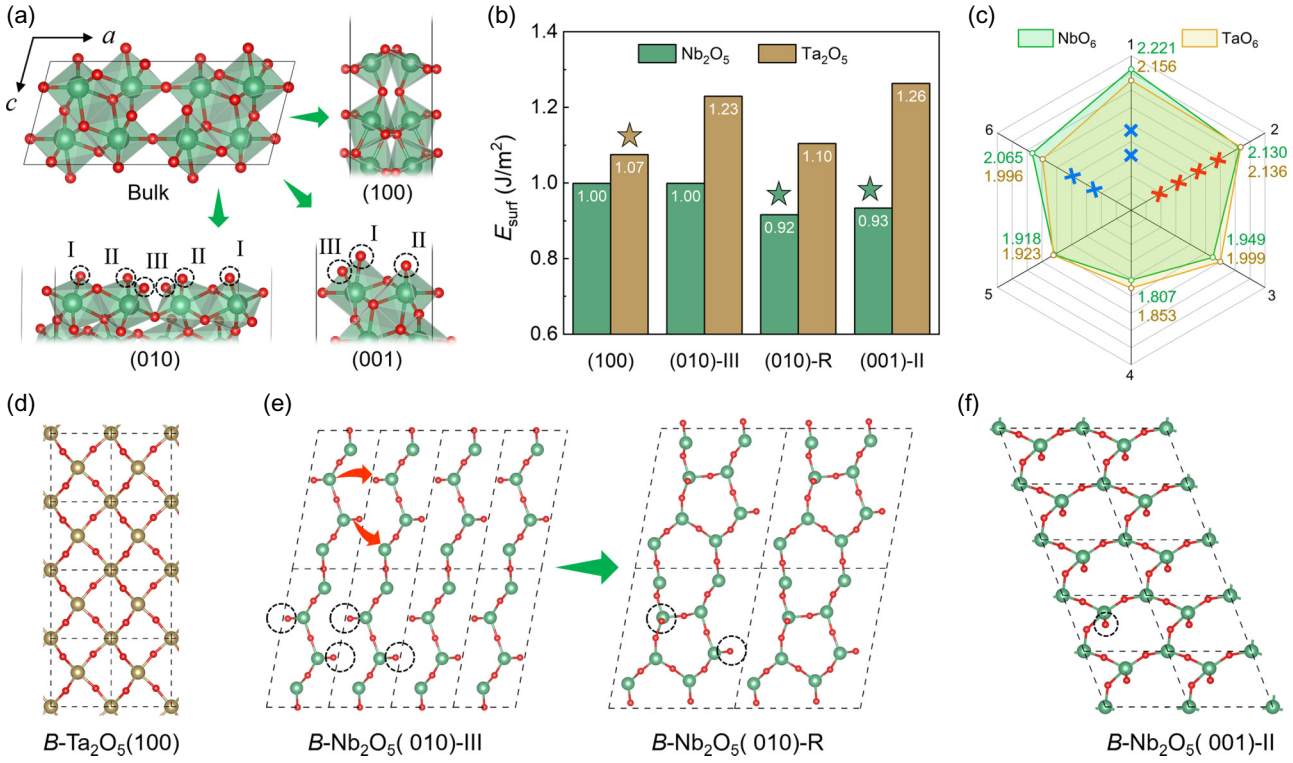

FIG. 1. Comparison of surface structures between B-Nb_2O_5 and B-Ta_2O_5. The Nb, Ta, and O atoms are represented by green, golden, and red balls, respectively. (a) Conventional cell of B-Nb_2O_5 and its possible surface structures. Here, I, II, and III denote different O terminations. (b) Surface energies of the most preferable configurations for each surface orientation, where (010)-R denotes the reconstructed (010) surface. The stars indicate the most stable surfaces, namely the (100) surface for B-Ta_2O_5, and the (010)-R and (001)-II surfaces for B-Nb_2O_5 which have almost identical surface energies. (c) $M-O$ ($M=$ Nb, Ta) bond lengths of the MO_6 octahedron in bulk B-Nb_2O_5 (green) and B-Ta_2O_5 (gold). The six axes represent the Nb–O (Ta−O) bonds of the NbO_6 (TaO_6) octahedron, with the numbers indicating the respective bond lengths depicted by the radial distance from the center. The red and blue "×" symbols indicate the bonds that need to be broken when forming the (100) and (001)-II surfaces, respectively. The dotted lines serve as visual guides. (d)–(f) Top views of surface morphologies for the most stable surfaces marked in (c). For clarity, only the outermost layer is drawn. The black dashed circles denote the positions of dangling O atoms.

surfaces, where II and III indicate the position of the terminal O atoms as shown in Fig. 1(a). After exploring possible surface reconstructions (see Appendix C), we find that the (010)-III surface tends to lower its energy by a 2×1 surface reconstruction, which is denoted as the (010)-R surface.

The surface energies for all four stoichiometric surfaces of B-Nb_2O_5 and B-Ta_2O_5 are given in Fig. 1(b). Notably, B-Nb_2O_5 exhibits a preference for either the reconstructed (010)-R surface or the (001)-II surface, while B-Ta_2O_5 primarily favors the (100) surface. As shown in Fig. 1(d), the B-Ta_2O_5(100) surface is remarkably smooth and lacks dangling O atoms. In contrast, the outermost Nb atoms on the B-Nb_2O_5(010)-R surface form alternating five- and seven-membered rings with bridging O atoms, resulting in two dangling O atoms. Additionally, the B-Nb_2O_5(001)-II surface features one dangling O atom on each six-membered ring, as depicted in Fig. 1(f). The stoichiometric nature of these surfaces ensures that these dangling O atoms are nonmagnetic and stable, as they do not have unpaired electrons.

As B-Nb_2O_5 and B-Ta_2O_5 share isomorphic bulk structures and their chemical properties are largely similar, it is intriguing to explore what drives their different surface preferences. To this end, we illustrate the M−O bond lengths within the MO_6 octahedrons of bulk B-M_2O_5 in Fig. 1(c). Figure 1(c) indicates that the Ta−O octahedron is more isotropic, with a smaller difference between the shortest (bond "4") and longest (bond "1") bond lengths (0.303 Å) compared to the Nb−O octahedron (0.414 Å). As indicated by the "×" symbols in Fig. 1(c), forming the (100) surface breaks four long "2" bonds, while forming the (001)-II surface breaks two "1" and two "6" bonds. Notably, the "1" and "6" bonds are significantly shorter (and thus stronger) in TaO_6 than in NbO_6, whereas the "2" bonds are nearly identical in both. This subtle difference between the local structures of B-Nb_2O_5 and B-Ta_2O_5 is sufficient to explain their distinct surface preferences, as

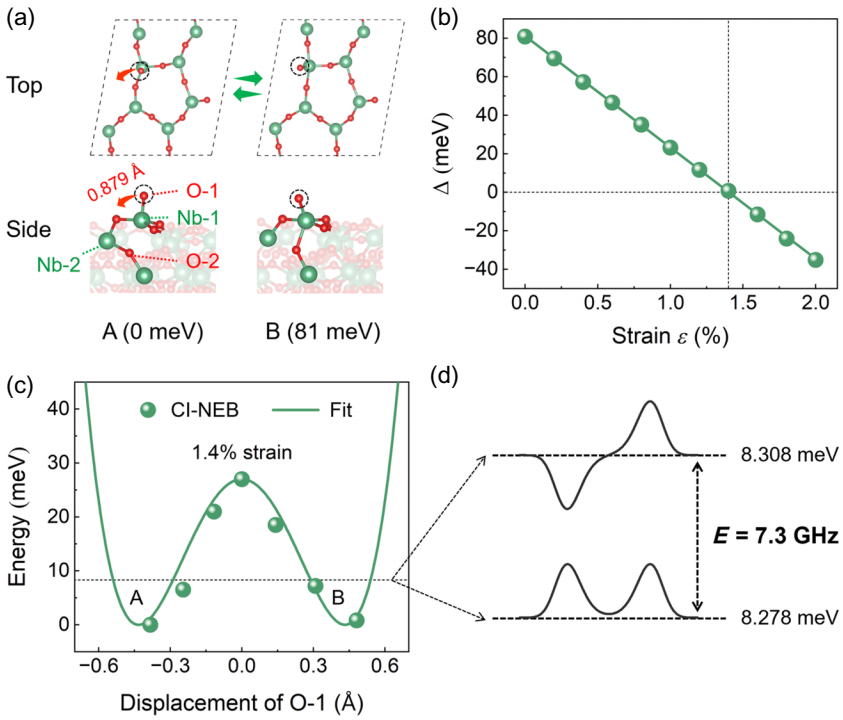

FIG. 2. A typical TLS formed on the (010)-R surface of B-Nb_2O_5. (a) Top and side views of the two locally stable states A and B. In the top view, only the outermost layer is drawn for clarity. The black dashed circles denote the positions of the rotated dangling O atoms. (b) Energy difference Δ between the two locally stable states as a function of the biaxial strain ε. (c) Double-well potential formed by structures A and B under a 1.4% strain. The green dots are the DFT energies calculated using the CI-NEB method, and the green line indicates the curve fitted using Eq. (1). (d) The tunneling splitting of the TLS, estimated by numerically solving the one-dimensional Schrödinger equation using the symmetric double-well potential in (c). The wavefunctions are indicated by black lines.

breaking the longer, weaker M−O bonds is energetically more favorable. As the (010)-R surface has dangling O atoms while the (100) surface has none, it is crucial to investigate whether dangling O atoms lead to the formation of structural TLSs and are hence responsible for the drastic differences in T_1 coherence times that are observed between Nb and Ta superconducting qubits.

After carefully moving the dangling O atoms and their neighbors in the supercell from the optimized geometries (see Appendix D for details), we successfully identified two structural TLSs on the B-Nb_2O_5(010)-R surface within the limit of the unit cell size. The first TLS (TLS-I) primarily involves the rotational motion of the dangling O atom around the perpendicular axis passing through the adjacent Nb-1 atom. As illustrated in Fig. 2(a), we find a double-well potential between two stable states, labeled as A and B, with an energy asymmetry of $\Delta = 81$ meV at zero strain. It is important to note that the rotation of O-1 alone is insufficient to establish the metastable state B. The transition from state A to B is characterized by a joint motion of two O atoms, a shift of 0.879 Å for the dangling O-1 atom and a shift of 0.485 Å for the underneath O-2 atoms. The joint process of bond breaking between O-2 and Nb-2 followed by the formation of a new bond between O-2 and Nb-1 is essential for stabilizing structure B.

The energy splittings of structural TLSs can be estimated from the asymmetry energy Δ, along with the tunneling matrix element Δ_0, as $E_{\mathrm{TLS}} = \sqrt{\Delta^2 + \Delta_0^2}$. Obviously, the value of $\Delta = 81$ meV is too large to be in resonance with superconducting qubits operating in the GHz region [6–8]; however, the amorphous nature of real surface oxides introduces random local strains, which are expected to significantly alter Δ [50], giving rise to a broad distribution of E_{TLS} values [7,8]. Indeed, we find that the value of Δ is very sensitive to the biaxial strain ε. As shown in Fig. 2(b), the TLS-strain coupling coefficient, $\gamma = (1/2)(\partial\Delta/\partial\varepsilon)$, is as large as 2.89 eV. This value is larger than that measured in Al superconducting qubits (0.1–1 eV) [51] but is close to that estimated for SiO_2 [52]. As a result, the double-well potential can become symmetric, as shown in Fig. 2(c), with a local stretching strain of 1.4%. Using the CI-NEB method [35], we can calculate the double-well potential for the transition path from A to B and fit it with a quartic polynomial:

$$U(x) = V - \frac{8V}{d^2}x^2 + \frac{16V}{d^4}x^4, \tag{1}$$

where V is the height of the energy barrier and x is the position of the dangling O-1 atom. From our fits, we can determine the distance between the two minima d (=0.865 Å) as well as the barrier V (=27 meV).

Now, we can estimate the minimum tunnel splitting of TLS-I by solving the one-dimensional (1D) Schrödinger equation for the symmetric double-well potential

$$-\frac{\hbar^2}{2m}\frac{d^2\psi}{dx^2} + U(x)\psi(x) = E\psi(x). \tag{2}$$

As an approximation, we use the mass of the dangling O atom, $m = 16$ u, to find the eigenvalues and wavefunctions of the two tunneling states. As shown in Fig. 2(d), the tunnel splitting is 7.3 GHz, which is in the experimental

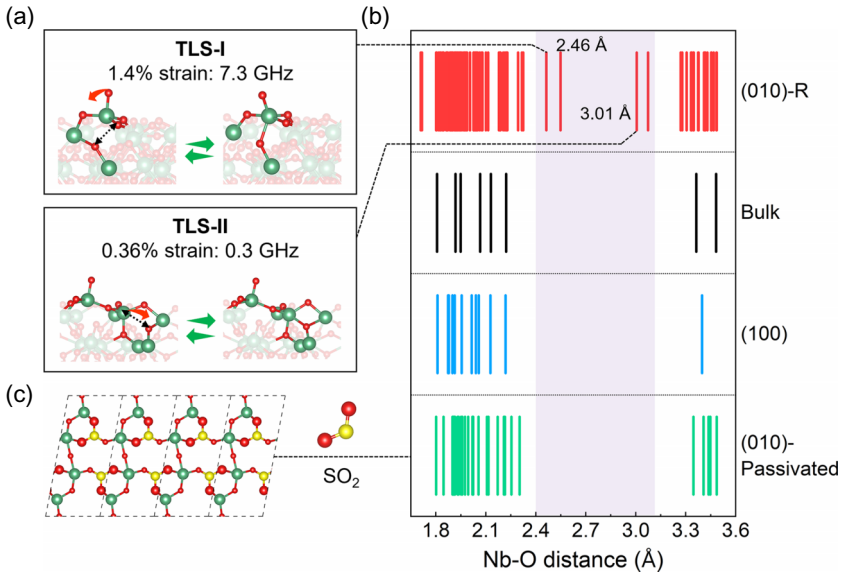

FIG. 3. Structures of two TLSs on B-Nb_2O_5 with a proposed way to reduce their density. (a) Two typical TLSs on the (010)-R surface of B-Nb_2O_5. The local strains that lead to $\Delta = 0$ are explicitly labeled, along with the corresponding tunnel splitting frequencies of the TLSs. The dotted arrows indicate the intermediate bonds marked in (b). (b) Distribution of the Nb–O bond lengths in the (010)-R surface, bulk, (100) surfaces, and SO_2-passivated (010) surface of B-Nb_2O_5. The light-purple area denotes the intermediate bonds, defined as bonds with lengths in the range from 2.4 to 3.1 Å. (c) Top view of the SO_2 passivated (010) surface, where the S and O atoms of SO_2 are represented by the yellow and larger red balls, respectively.

range. The motion of the dangling O atom, with a negative charge of $-0.8e$ from a Bader charge analysis [53], leads to a significant change in the electric dipole moment of 5.33 Debye between states A and B. This is consistent with experimental observations, which are typically distributed around 2.8 and 8.3 Debye [50,54].

Another structural TLS on the B-Nb_2O_5(010)-R surface is denoted as TLS-II [see Fig. 3(a)], which involves a Nb atom moving close to the dangling O atom, even though this O atom seldom moves. A local strain of 0.36% produces a symmetric double-well potential with barrier width $d = 0.485$ Å and energy-barrier height $V = 28$ meV. As the motion of Nb plays a pivotal role in the formation of TLS-II, we use the atomic mass of Nb atoms ($m = 92.9$ u) in solving the 1D Schrödinger equation with a symmetric double-well potential. This gives a tunnel splitting of 0.3 GHz and an electric dipole moment change of 5.00 Debye for TLS-II.

Both types of structural TLS involve breaking Nb–O bonds, which generally involves large energies. This is puzzling considering the relatively low energy barriers (of the order of tens of meV) of their double-well potential profiles. To explain this, Fig. 3(b) illustrates the distribution of Nb−O bond lengths across various surfaces: (010)-R, (100), and within-bulk B-Nb_2O_5. As highlighted by the lightly shaded purple area in Fig. 3(b), there is a significant gap between the first- and second-neighbor bond-length groups in bulk B-Nb_2O_5 and on the smooth (100) surface, indicating their strong structural stability; however, for the (010)-R surface, which features dangling O atoms, several intermediate bond lengths fall into the aforementioned gap, as indicated by dashed lines in Fig. 3. These lengths range from 2.4 to 3.1 Å, suggesting that these O (Nb) atoms are only loosely bound and may jump between different Nb (O) atoms. The presence of intermediate bond lengths indicates weak Nb−O bonds on these surfaces, which can be broken or reformed with relatively low energies, thus accounting for the small energy barriers of the TLSs. The emergence of these intermediate bonds is closely linked to the presence of dangling O atoms, which are attached to only one Nb atom and can thereby extract more electrons from it than is typically seen in the bulk structure. Consequently, the Nb atoms beneath the surface cannot supply enough electrons to the subsurface O atoms, resulting in overall weaker Nb−O bonds in the surface region.

The observation that the surface energy of B-Ta_2O_5 (010)-R is also close to that of B-Ta_2O_5 (100) in Fig. 1(b) might suggest the presence of dangling O atoms and structural TLSs on Ta-based qubits as well; however, DFT calculations reveal notable differences between the TLS configurations on B-Ta_2O_5(010)-R and B-Nb_2O_5(010)-R, particularly regarding the heights of their potential barriers. The barrier height of TLS-II becomes 39 meV on B-Ta_2O_5(010)-R, much higher than that on B-Nb_2O_5(010)-R, at $V = 28$ meV (see Appendix D). Furthermore, the greater atomic mass of Ta ($m = 180.9$ u) compared to Nb significantly reduces the tunneling probability and TLS energy

splitting, according to the Wentzel–Kramers–Brillouin (WKB) theory [55], which gives $E_{\mathrm{TLS}} \propto e^{-d\sqrt{2mV/\hbar^2}}$. Using parameters derived from DFT calculations, we find that the tunnel splitting of TLS-II on the B-Ta_2O_5 (010)-R surface is only 66 kHz. This value is significantly lower than the GHz region relevant for the operating frequencies of quantum computing devices.

We can now explain why Ta-based qubits may significantly outperform those based on Nb. The primary reason is that Ta_2O_5 features a highly stable and smooth (100) surface, which hosts far fewer defect-associated structural TLSs. This characteristic is crucial because TLSs are known sources of quantum decoherence and noise in qubits. The second key factor contributing to the superior performance of Ta-based qubits involves several intertwined physical properties: greater atomic mass and higher potential-energy barriers. These properties significantly lower the tunneling probability and drive the tunneling splitting of probable TLSs far below the frequency range of qubit operations. Consequently, the operational efficiency of Ta-based qubits is substantially enhanced, making them more promising for quantum computing applications.

Finally, the influence of structural TLSs on the surfaces of oxides can be mitigated by employing dc electric fields. This approach leverages the electric dipole moments associated with TLSs [50,54,56,57]. As expected, the asymmetry energies of two distinct types of TLS vary linearly with the applied electric field [see Appendix E]. Using the field-dependent potential wells in Eq. (2), we find that E_{TLS} can be effectively driven out of the GHz range (see Appendix E). Additionally, we calculate the resonant dielectric absorption coefficient [58], which is proportional to the square of the dipole moment (see Appendix E). It is important to note that although applying an electric field can shift certain TLSs out of resonance, it may inadvertently bring other previously nonresonant TLSs into the GHz range [50]. Therefore, the effectiveness of using a dc field appears to be uncertain, depending on the specific TLS spectra of the materials involved. Nonetheless, it is encouraging that a very recent experiment [59] reported a significant 23% improvement in T_1 of a superconducting qubit by applying dc electric fields.

Another potential method for reducing the density of TLSs on oxide surfaces involves eliminating dangling O atoms through chemisorption. After exploring various gases for this purpose (see Appendix E for CO adsorption and further details), we find that the adsorption of SO_2 is particularly effective, especially on the (010)-R surface of Nb. Chemisorption of SO_2 can effectively "cap" the dangling O atoms, thereby stabilizing the surface and reducing the number of sites where TLSs can form. As depicted in Fig. 3(c), SO_2 molecules may bridge the dangling O atoms and their Nb neighbors, restricting their motion to form metastable configurations. The adsorption energy of SO_2 on B-Nb_2O_5(010)-R is high: 1.58 eV per molecule. This stable chemical intervention results in the elimination of intermediate bond lengths, as illustrated in the bottom panel of Fig. 3(b). As a result, all atoms are effectively

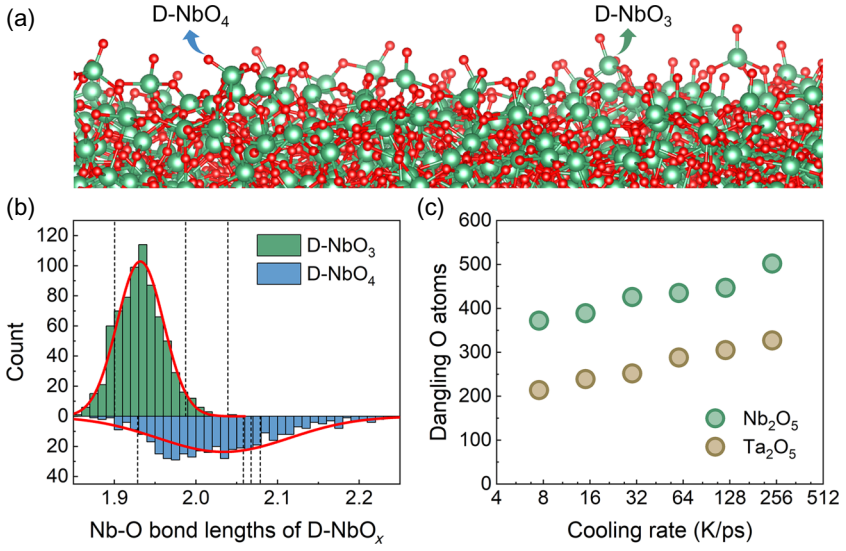

FIG. 4. Simulations of amorphous surfaces (approximately 100×100 Å^2) for Nb_2O_5 and Ta_2O_5. (a) Local surface morphology of amorphous Nb_2O_5, generated with a cooling rate of 7.5 K/ps. The Nb and O atoms are represented by green and red balls, respectively. The surface is dominated by D-NbO_3 and D-NbO_4 patterns, where D represents the dangling O atom. (b) Distribution of Nb−O bond lengths in the D-NbO_3 and D-NbO_4 patterns on the amorphous surface. The red solid lines represent Gaussian distribution fits, while the black dashed lines indicate corresponding bond lengths on the unstrained B-Nb_2O_5(010)-R surface. (c) Numbers of dangling O atoms on amorphous Nb_2O_5 and Ta_2O_5 surfaces, generated with different cooling rates.

frozen in the ground-state geometry, and the TLS density is thus significantly reduced.

So far, our conclusions are derived from the crystalline phases of Nb_2O_5 and Ta_2O_5 surfaces; however, these conclusions should also be applicable to amorphous surfaces, as the formation of structural TLSs is determined by local atomic environments rather than long-range order. To test this hypothesis, we used MD simulations with MLFFs [39–41] to create amorphous surfaces of Nb_2O_5 and Ta_2O_5 in large supercells (approximately 100×100 Å^2), employing the standard melt-and-quench method [42]. This approach allows us to model more realistic amorphous surfaces with near *ab initio* accuracy.

The results, shown in Fig. 4, indicate that the surface morphology of amorphous Nb_2O_5 [Fig. 4(a)] still exhibits a high density of dangling O atoms (1.87/nm^2). Despite the structural complexity, the local environments around these O atoms closely resemble the locally stable TLS states A and B identified in the crystalline model, labeled as D-NbO_3 or D-NbO_4 in Fig. 4(a) ("D" represents the dangling O atom). The Nb−O bond lengths for each case follow an approximate Gaussian distribution, as shown in Fig. 4(b), suggesting a wide range of local strains. Based on these results, we estimate a TLS density of approximately $\sigma \approx 3.9/(\text{GHz } \mu\text{m}^2)$, as detailed in Appendix F. This estimated density falls within the range of experimental values observed in $Al/AlO_x/Al$ and $Nb/AlO_x/Nb$ junctions, reported to be between 0.4 and 4.4/(GHz μm^2) [6], confirming that dangling O atoms on Nb_2O_5 surfaces significantly contribute to the formation structural TLSs. Using the same simulation procedure, as also shown in Fig. 4(c), we find that the number of dangling O atoms on the amorphous Ta_2O_5 surface is roughly half that observed on amorphous Nb_2O_5 surfaces, consistent with the observations from the crystalline phase.

IV. CONCLUSIONS

In summary, our study provides a new perspective on the disparities in T_1 relaxation times between Nb and Ta superconducting qubits, focusing on the role of structural TLSs at their vacuum-oxide interfaces. Through crystalline modeling and energetic analyses, we find that Nb_2O_5 tends to prefer rougher surfaces that host dangling O atoms, contributing to the formation of structural TLSs and reducing the coherence times of Nb qubits. In contrast, Ta_2O_5 favors smoother surfaces where dangling O atoms are rare, leading to fewer TLS-related losses and, consequently, longer coherence times in Ta qubits. Additionally, the greater atomic mass of Ta helps lower the tunnel splitting, shifting TLSs away from the GHz frequency range of qubits.

The presence of a large number of dangling O atoms on Nb_2O_5 and the significant reduction of this number on Ta_2O_5 are further confirmed by large-scale MD simulations of their amorphous phases, demonstrating the applicability of our findings to real materials. These insights highlight the critical impact of surface conditions—specifically, the presence or absence of dangling O atoms—on the performance of superconducting qubits.

Moreover, we explore promising strategies for mitigating the deleterious effects of structural TLSs on oxide surfaces of superconducting qubits. Applying a dc electric field and passivating the surface with SO_2 gas have both shown potential for modifying or eliminating structural TLSs on Nb and Ta qubit surfaces. These approaches could significantly advance the development of superconducting qubits by improving their coherence times and overall operational stability, paving the way for more reliable and effective quantum computing technologies.

ACKNOWLEDGMENTS

This work was supported by the USA-DOE, Office of Basic Energy Science (Grant No. DE-FG02-05ER46237). This work was also supported in part by the US Army Research Office in collaboration with the Laboratory for Physical Sciences (Grant No. W911NF24C0001). Calculations were conducted on the High-Performance Community Computing Cluster at UC Irvine and were also partially performed on supercomputers at The National Energy Research Scientific Computing Center.

APPENDIX A: PHASE DIAGRAMS OF Nb AND Ta OXIDES

Experiments have found that the native oxide layer of Nb has a complex composition. As schematically depicted in Fig. 5(a), it is composed of multiple suboxides (NbO and NbO_2) close to the Nb side, followed by Nb_2O_5 as the outermost layer [18–21,27]. In comparison, the native oxide layer of Ta consists solely of Ta_2O_5 [26] [Fig. 5(b)].

This is also confirmed by our DFT phase diagram calculations. We calculate the Gibbs free energy of formation (ΔG) for different Nb and Ta oxides using

$$\Delta G = \frac{1}{x+y}\left[E_{M_xO_y} - xE_M - y\left(\frac{1}{2}E_{O_2} + \Delta\mu_O\right)\right]. \tag{A1}$$

Here, M represents Nb or Ta; $E_{M_xO_y}$, E_M, and E_{O_2} are the calculated total energies of bulk M oxides, the bulk M metal, and the O_2 molecule, respectively; and $\Delta\mu_O$ is the chemical potential of O with respect to half the total energy of an O_2 molecule. For each M oxide, we consider various polymorphic forms and select the most stable one, i.e., MO, MO_2, and M_2O_5 with space groups $Pm\bar{3}m$, $I4_1/a$, and $C2/c$, respectively. As shown in Fig. 5(c), when $\Delta\mu_O$ changes from O-rich to Nb-rich conditions, the most stable phase of Nb oxides varies from Nb_2O_5 to NbO_2, and then to NbO. In contrast, the most stable phase of Ta oxides

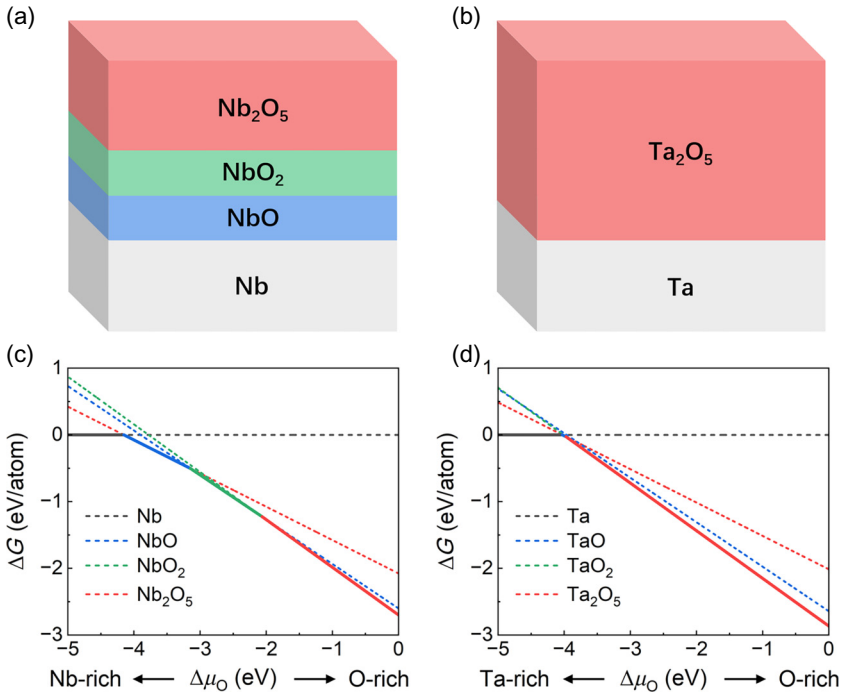

FIG. 5. (a),(b) Schematic diagrams of the native oxide layers of Nb and Ta. The Nb oxides are composed of multiple components, including NbO, NbO_2, and Nb_2O_5, while the Ta oxides consist solely of Ta_2O_5. (c),(d) Phase diagrams of Nb and Ta oxides, obtained by comparing the Gibbs free energy of formation (ΔG) under different O chemical potentials ($\Delta\mu_O$).

is always Ta_2O_5, regardless of the value of the chemical potential of O.

APPENDIX B: SELECTION OF THE REPRESENTATIVE STRUCTURES FOR Nb_2O_5 AND Ta_2O_5

As discussed in the main text, we adopt the crystalline structures of Nb_2O_5 and Ta_2O_5 to investigate the oxides of Nb and Ta at the vacuum-oxide interface, since it is difficult to model the real amorphous structures. The crystalline structures of Nb_2O_5 and Ta_2O_5, however, exhibit a number of polymorphs. The polymorph we select should have high energetic stability, as well as a simple structure to facilitate our theoretical simulations. Based on these considerations, we selected one specific polymorph as the representative model for each metal oxide.

Nb_2O_5 is known to crystallize in various polymorphic forms [60], such as the B (or ζ), H, N, R, M, and Z phases; their relative stabilities are compared in Fig. 6 using the DFT-calculated formation energies. Although H-Nb_2O_5 is believed to be the most thermodynamically stable phase at high temperatures [61,62], our calculations indicate that B-Nb_2O_5 is the most stable phase at low temperatures, in accordance with previous DFT studies [62]. Additionally, the primitive cell of H-Nb_2O_5 contains 98 atoms, while B-Nb_2O_5 has only 14 (28) atoms in its primitive (conventional) cell, which is more suitable for DFT calculations; we therefore adopt B-Nb_2O_5 to investigate the surface oxides of Nb films. The calculated lattice parameters of B-Nb_2O_5 are listed in Table I, and these show deviations of less than 0.7% from the experimental values.

For Ta_2O_5, our calculation indicates that B-Ta_2O_5 is the most stable phase (Fig. 6), consistent with recent DFT studies [63]. Hence, we use B-Ta_2O_5 to mimic surface oxide on Ta films. It is important to note that we have the same polymorphic form for Nb_2O_5 and Ta_2O_5, which allows us to reveal the difference between Nb and Ta more

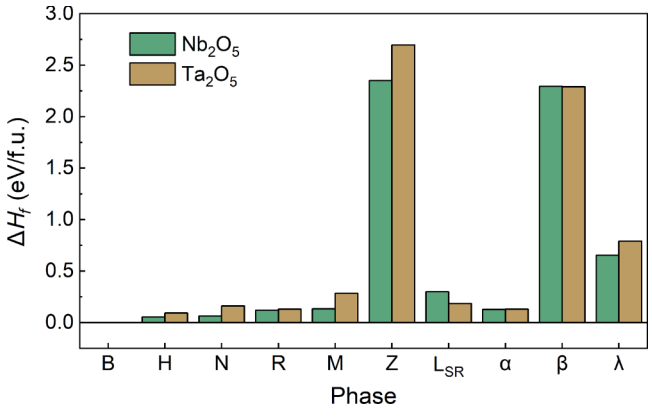

FIG. 6. Formation energies per formula unit (f.u.) of various Nb_2O_5 and Ta_2O_5 polymorphs with respect to their B-phases. The zero-point energy and finite-temperature effects are not taken into account.

TABLE I. Calculated lattice parameters of B-Nb_2O_5 and B-Ta_2O_5. The experimental values are also listed for comparison.

Oxide		a (Å)	b (Å)	c (Å)	α	β	γ
B-Nb_2O_5	Calc.	12.82	4.89	5.57	90°	104.7°	90°
	Expt. [48]	12.74	4.88	5.56	90°	105.0°	90°
B-Ta_2O_5	Calc.	12.89	4.89	5.55	90°	103.8°	90°
	Expt. [49]	12.79	4.85	5.53	90°	104.3°	90°

intrinsically without being concerned with structural differences. The calculated lattice parameters for B-Ta_2O_5 are listed in Table I, which shows deviations of less than 0.9% from the experimental values.

APPENDIX C: SURFACE STRUCTURES OF B-Nb_2O_5 AND B-Ta_2O_5

The surface structures of the metal oxides are simulated using slab models. We start from fully relaxed bulk structures and cleave them into slabs in such a way that the surfaces at each side are equivalent. The slab thicknesses are chosen to be greater than 10 Å, which is thick enough to avoid interactions between the two sides. A vacuum space of 15 Å is inserted along the z axis to eliminate interactions between the periodically repeated images. The surface energy is calculated using

$$E_{\text{surf}} = \frac{1}{2A}(E_{\text{slab}} - n_M\mu_M - n_{\text{O}}n_{\text{O}}), \tag{C1}$$

where E_{slab} is the total energy of the slab; μ_{M} and μ_{O} are the chemical potentials of M atoms ($M = \text{Nb, Ta}$) and O atoms, respectively; n_M and n_{O} are their corresponding atom numbers; and A is the surface area. The values of μ_M and μ_{O} are dependent on experimental conditions. At the vacuum-oxide interface, the O_2 gas in the atmosphere acts as a reservoir for the O in the metal oxides, and thus the chemical potential of O with respect to $1/2E_{O_2}$ can be expressed as

$$\Delta\mu_{\text{O}}(T,P) = \mu_{\text{O}}(T,P) - \frac{1}{2}E_{O_2} = \frac{1}{2}[H(T,P) - TS(T,P)], \tag{C2}$$

where $E(O_2)$ is the DFT-calculated total energy of an O_2 molecule, and H and S are the enthalpy and entropy of the O_2 gas phase at temperature T and pressure P. Given that the oxide layers are formed under ambient conditions, we can simply use the tabulated values [64] for O_2 at standard states ($H_0 = 8.68$ kJ mol^{-1}, $S_0 = 205.138$ J mol^{-1}·K^{-1} at $T_0 = 298.15$ K, $P_0 = 1$ bar), which yields $\Delta\mu_{\text{O}} = -0.272$ eV. The chemical potential of the metal element μ_M can then be determined via the thermodynamic stability conditions

$$\begin{aligned} E_{Nb_2O_5} &= 2\mu_{\text{Nb}} + 5\mu_{\text{O}}, \\ E_{Ta_2O_5} &= 2\mu_{\text{Ta}} + 5\mu_{\text{O}}. \end{aligned} \tag{C3}$$

Using Eqs. (C1) and (C3), one can find that for stoichiometric surfaces, the surface energy is a constant regardless of the chemical potentials, as it can be written as

$$E_{\text{surf}} = \frac{1}{2A}(E_{\text{slab}} - nE_{\text{bulk}}), \tag{C4}$$

where E_{bulk} is the energy of the bulk phase per unit cell and n is the number of unit cells that the slab contains.

We consider the (100), (010), and (001) surfaces for B-Nb_2O_5 and B-Ta_2O_5, and take into account all possible terminations, either stoichiometric or nonstoichiometric. It is worth emphasizing that B-Nb_2O_5 has several important "hidden" surface configurations, which were all neglected in previous DFT studies [65]. Here, we take its stoichiometric surface as an example. As displayed in Fig. 7, the (100) orientation has the simplest surface, with only one stoichiometric configuration. In comparison, the (010) orientation shows much more complex surface structures. As displayed in Fig. 7(c), disconnecting the NbO_6 octahedra

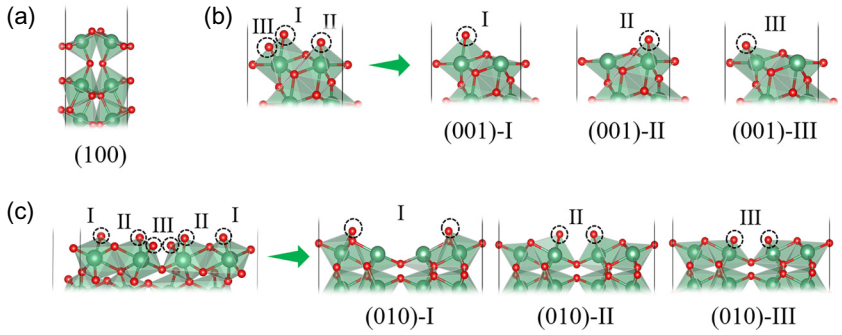

FIG. 7. Structures of the seven possible stoichiometric surfaces of B-Nb_2O_5. The Nb and O atoms are represented by green and red balls, respectively. The black dashed circles indicate the positions of dangling O atoms.

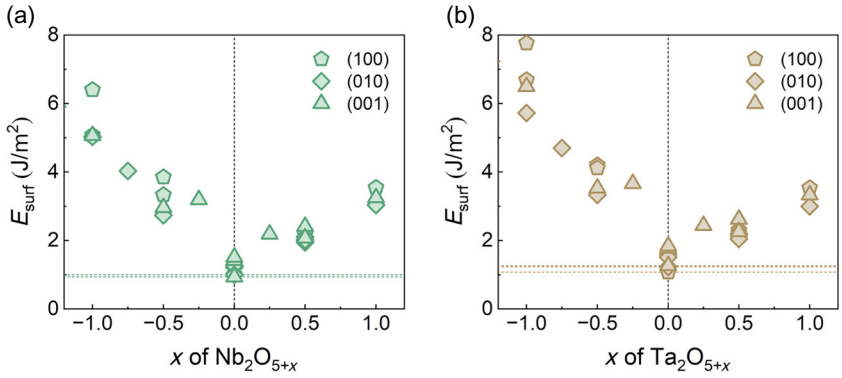

FIG. 8. Surface energies of all possible surfaces for (a) B-Nb_2O_5 and (b) B-Ta_2O_5. Different polygons represent different surface orientations. The horizontal dashed lines indicate the most stable configuration of each surface orientation.

along the (010) direction leaves six O atoms on its surface, which are located at the high (I), medium (II), and low positions (III). To form a stoichiometric surface, only two O atoms should be retained, leading to three surface configurations, namely (010)-I, -II, and -III. Likewise, the (001) orientation has three stoichiometric surfaces, as shown in Fig. 7(b), where the outermost O atom can be stabilized at three different positions, denoted as (001)-I, -II, and -III.

In addition to the seven stoichiometric surfaces noted above, we construct another 26 possible nonstoichiometric surfaces for B-Nb_2O_5 and B-Ta_2O_5. The surface energies of all these 33 surfaces under ambient conditions are calculated using Eqs. (C1)–(C4), and the results are shown in Fig. 8. We find that the most preferable configurations for each surface orientation are all stoichiometric for both B-Nb_2O_5 and B-Ta_2O_5. Specifically, they are the (100), (010)-III, and (001)-II surfaces, as displayed in Fig. 7. Note that the (001)-II surface was overlooked in previous DFT studies [65], presumably because its construction is not straightforward, as mentioned earlier.

We then examine whether the three surfaces will further lower their energies by surface reconstruction. For the (100) and (001)-II surfaces, we manually construct various reconstructed structures, but they spontaneously

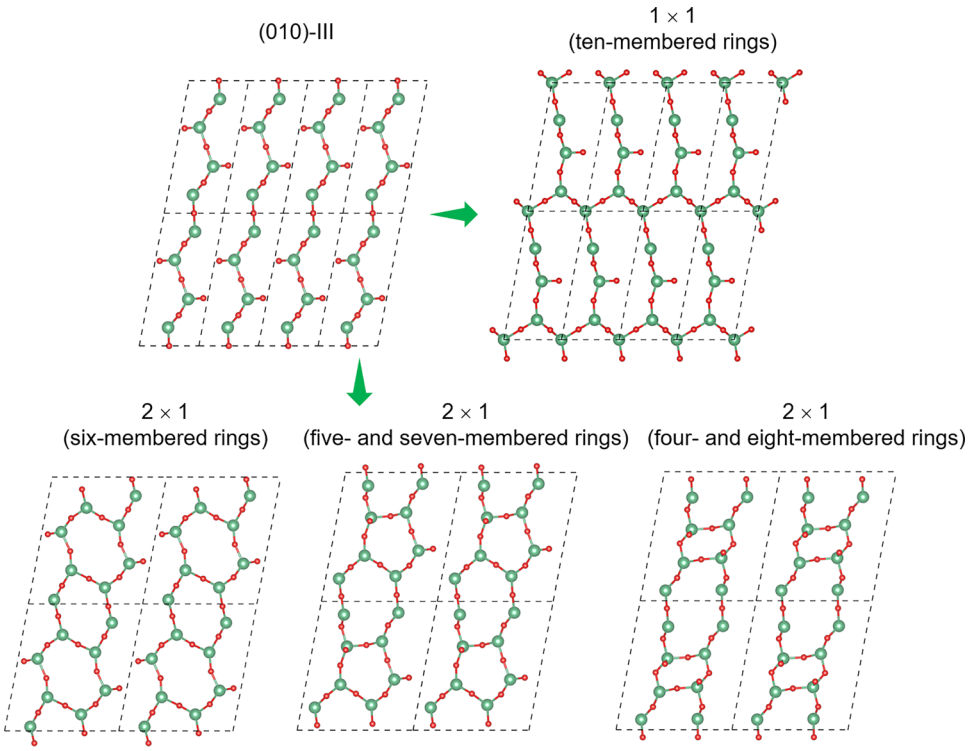

FIG. 9. Possible surface reconstructions for the (010)-III surface.

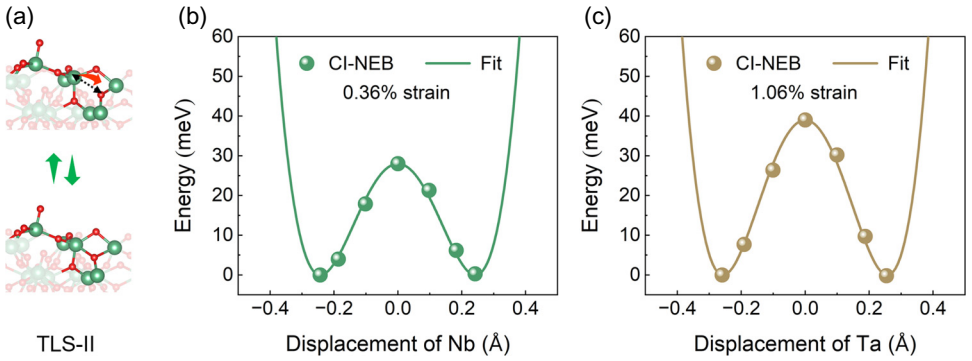

FIG. 10. Double-well potentials of TLS-II on the B-Nb_2O_5 and B-Ta_2O_5 surfaces. (a) Side view of the two locally stable states in TLS-II. The metal (Nb or Ta) and O atoms are represented by green and red balls, respectively. The tunneling between the two states mainly involves the hopping of metal atoms. (b),(c) Double-well potentials of TLS-II at 0.36% and 1.06% strain for B-Nb_2O_5 and B-Ta_2O_5, respectively.

relax back, indicating that reconstruction is unfavored. Conversely, for the (010)-III surface, we identify various reconstructed structures, as shown in Fig. 9, where the outermost Nb atoms form different rings through the bridging of O atoms. The structure with the lowest energy is formed by alternating five- and seven-membered rings, which lower the surface energy of the (010)-III surface by 0.083 and 0.125 J/m^2 for B-Nb_2O_5 and B-Ta_2O_5, respectively.

APPENDIX D: TLS ON B-Nb_2O_5 AND B-Ta_2O_5 SURFACES

1. Procedures for searching for possible TLSs

To identify possible TLSs that are produced by the dangling O atoms, we follow the procedure described below. We first build a large enough supercell and rotate one dangling O atom away from its original position by 1 Å, without changing the Nb−O bond length. The rotation azimuthal angles are varied from 0° to 360° with a step of 30°. Next, we fix the rotated O atom, as well as the Nb atom that is linked to it, and perform a precursive relaxation. After that, we free all the atoms and run a final relaxation. Note that the precursive relaxation of fixing the O and Nb atoms is essential to obtain the final metastable structure. This is because the rotation of a dangling O atom alone cannot form a stable state and will spontaneously relax back. The precursive relaxation can drive the other atoms to the optimized positions, which may help stabilize the new position of the rotated dangling O atom.

2. TLS-II on Nb_2O_5 and Ta_2O_5 surfaces

The double-well potentials of TLS-II on B-Nb_2O_5 and B-Ta_2O_5 surfaces are given in Fig. 10, and the corresponding tunnel splittings are listed in Table II. It can be seen that the tunnel splitting of TLS-II on B-Ta_2O_5 is almost zero (66 kHz)—far below the typical operating frequency (1–10 GHz) of superconducting qubits—and it therefore has negligible effect on the coherence times of Ta qubits. This is mainly caused by the heavier atomic mass of Ta atoms. As shown in Fig. 10(a), TLS-II primarily involves the hopping of metal atoms (Nb or Ta). According to the Wentzel–Kramers–Brillouin (WKB) theory [55], the tunnel splitting of a symmetric double-well potential is very sensitive to the atomic mass m with $E_{\mathrm{TLS}} \propto e^{-d\sqrt{2mV/\hbar^2}}$, where d and V are the distance between the two minima and the barrier height, respectively. Since the atomic mass of Ta (180.9 u) is almost double that of Nb (92.9 u), the tunnel splitting of TLS-II can be significantly different on B-Nb_2O_5 and B-Ta_2O_5 surfaces. In fact, by simply changing the atomic mass from Nb to Ta in TLS-II of B-Nb_2O_5 [Fig. 10(b)], the tunnel splitting is dramatically reduced by a factor of 1000, from 0.3 to 0.003 GHz, as show in Table II. Additionally, the barrier height of TLS-II on B-Ta_2O_5 is higher, which further reduces the tunnel splitting to 6.6×10^{-5} GHz. Hence, the greater atomic mass of Ta also plays an important role in the longer coherence time of Ta qubits.

APPENDIX E: METHODS FOR REDUCING THE TLS DENSITY

1. Electric-field tuning of the TLSs

Due to the electric dipole moments associated with TLS-I and TLS-II, their asymmetric energies can be effectively tuned using external dc electric fields, as illustrated in Fig. 11(a). As a result, the tunnel splittings can be driven out of the GHz range, as shown in Fig. 11(b). In this figure, the circle sizes are proportional to the dielectric absorption coefficient $\alpha \propto \mathbf{p}'^2$ [58] where $\mathbf{p}' = \langle\psi_+|\mathbf{D}|\psi_-\rangle$. Here, $|\psi_+\rangle$ and $|\psi_-\rangle$ are the numerically solved wavefunctions of the TLS, and $\mathbf{D}$ is the electric dipole moment. This is equivalent to $\alpha \propto \Delta_0^2/E_{\mathrm{TLS}}^2$ as demonstrated below.

TABLE II. Calculated parameters of the double-well potential of TLS-II on the B-Nb_2O_5 and B-Ta_2O_5 surfaces, and the corresponding tunnel splitting E_{TLS}. The third row (Nb → Ta) shows the results of simply changing the atomic mass from Nb to Ta in TLS-II of the B-Nb_2O_5 surface.

System	Barrier width (Å)	Barrier height (meV)	Atomic mass (u)	E_{TLS} (GHz)
B-Nb_2O_5	0.485	28	92.9	0.3
Nb → Ta	0.485	28	180.9	0.003
B-Ta_2O_5	0.514	39	180.9	6.6×10^{-5}

In the left and right well basis, the Hamiltonian of a TLS in the perturbing electric field can be expressed as [50,56]

$$H = H_0 + \mathbf{D}\cdot\mathbf{F} = \frac{1}{2}\begin{pmatrix} \Delta + \mathbf{D}\cdot\mathbf{F} & \Delta_0 \\ \Delta_0 & -\Delta - \mathbf{D}\cdot\mathbf{F} \end{pmatrix}, \quad \text{(E1)}$$

where Δ is the asymmetry energy, Δ_0 is the tunneling matrix element, $\mathbf{D}$ is the electric dipole moment, and $\mathbf{F}$ is the external electric field. We now transition to the TLS basis of

$$\begin{aligned} |\psi_+\rangle &= \sin\left(\frac{\theta}{2}\right)|L\rangle + \cos\left(\frac{\theta}{2}\right)|R\rangle, \\ |\psi_-\rangle &= \cos\left(\frac{\theta}{2}\right)|L\rangle + \sin\left(\frac{\theta}{2}\right)|R\rangle. \end{aligned} \quad \text{(E2)}$$

Here, the mixing angle θ is defined as $\tan\theta = \Delta_0/\Delta$. The Hamiltonian (E1) is then transformed to

$$\begin{aligned} H &= \frac{1}{2}\begin{pmatrix} \sqrt{\Delta^2+\Delta_0^2} & 0 \\ 0 & -\sqrt{\Delta^2+\Delta_0^2} \end{pmatrix} \\ &\quad + \frac{1}{2}\frac{1}{\sqrt{\Delta^2+\Delta_0^2}}\begin{pmatrix} \Delta\mathbf{D}\cdot\mathbf{F} & -\Delta_0\mathbf{D}\cdot\mathbf{F} \\ -\Delta_0\mathbf{D}\cdot\mathbf{F} & -\Delta\mathbf{D}\cdot\mathbf{F} \end{pmatrix} \\ &= \frac{1}{2}\begin{pmatrix} E & 0 \\ 0 & -E \end{pmatrix} + \frac{1}{2}\begin{pmatrix} \mathbf{p} & 2\mathbf{p}' \\ 2\mathbf{p}' & -\mathbf{p} \end{pmatrix}\cdot\mathbf{F}, \end{aligned} \quad \text{(E3)}$$

where

$$\mathbf{p} = \frac{\Delta\mathbf{D}}{\sqrt{\Delta^2+\Delta_0^2}}, \mathbf{p}' = -\frac{1}{2}\frac{\Delta_0\mathbf{D}}{\sqrt{\Delta^2+\Delta_0^2}}. \quad \text{(E4)}$$

It is known that the dielectric absorption coefficient α is proportional to the square of $\mathbf{p}'$ [58]. We then obtain

$$\alpha \propto \mathbf{p}'^2 = \frac{1}{4}\frac{\Delta_0^2}{\Delta^2+\Delta_0^2}\mathbf{D}^2 \propto \frac{\Delta_0^2}{E_{TLS}^2}. \quad \text{(E5)}$$

2. Gas molecules for passivating the dangling O atoms

We examined several simple gases to passivate the dangling O atoms on the B-Nb_2O_5(010)-R surface, including carbon monoxide (CO), carbon dioxide (CO_2), sulfur dioxide (SO_2), carbonyl sulfide (OCS), and dinitrogen monoxide (N_2O). We excluded nitrogen monoxide (NO) and nitrogen dioxide (NO_2) due to their magnetic moments of 1 μ_B, which could introduce additional magnetic flux noise.

Our investigations revealed that CO_2, OCS, and N_2O do not effectively passivate the dangling O atoms, as they exhibit weak adsorption on the Nb_2O_5 surface with adsorption energies of −0.56, −0.63, and −0.63 eV/molecule, respectively.

Conversely, both CO and SO_2 demonstrate strong binding to the dangling O atoms. The CO molecule bridges between a dangling O atom and a neighboring Nb atom, forming an O−C−O−Nb chain, as shown in Fig. 12(a). Adjacent chains can connect via a C−C bond, which helps to lower the overall energy. Despite

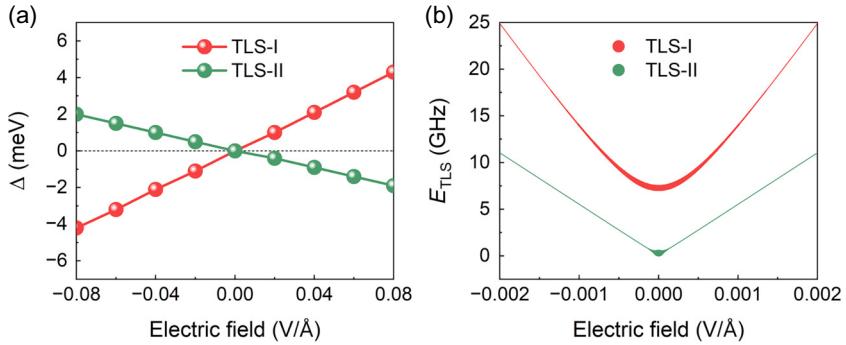

FIG. 11. (a) Asymmetry energy Δ as a function of external dc electric field for the two typical TLSs. (b) Tunneling splitting of the two TLSs tuned by electric fields. The circle sizes are proportional to the dielectric absorption coefficient.

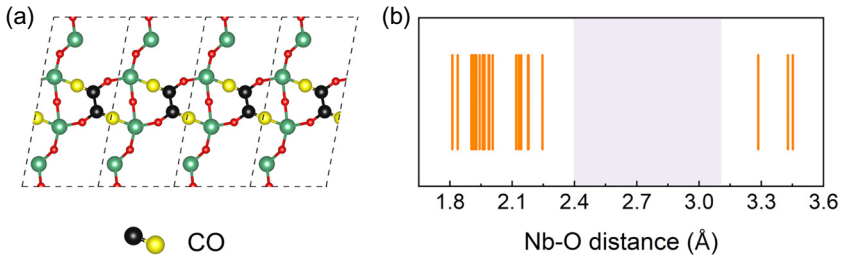

FIG. 12. (a) Top view of the CO-passivated (010) surface of B-Nb_2O_5, where the C and O atoms of CO are represented by black and yellow balls, respectively. (b) Distribution of the Nb−O bond lengths in the CO-passivated (010) surface of B-Nb_2O_5. The light-purple area indicates that the intermediate bond lengths are eliminated by CO passivation.

this, we ruled out CO for two reasons: its adsorption energy of −0.75 eV/molecule is significantly weaker than that of SO_2 (−1.58 eV/molecule), and forming such an ordered pattern is challenging. Additionally, excess CO on the "passivated" surface has a similar adsorption energy (−0.66 eV/molecule) and could potentially generate new TLSs.

Ultimately, SO_2 emerged as a superior passivator for the dangling O atoms. Its high adsorption energy of −1.58 eV/molecule indicates a strong and stable binding, effective even at room temperature. Furthermore, additional SO_2 molecules adsorbed on the "passivated" surface show a much weaker interaction (−0.37 eV/molecule), suggesting that they can be readily desorbed by heating. Based on these findings, we selected SO_2 for passivation purposes. Other gases may also be suitable, and further studies could explore their effectiveness.

APPENDIX F: ESTIMATION OF THE TLS DENSITY ON AMORPHOUS Nb_2O_5 SURFACES

Direct calculation of the TLSs on amorphous Nb_2O_5 surfaces is challenging due to the large system size (approximately 100 × 100 Å^2 with 8064 atoms in our simulations). Therefore, we estimate the TLS associated with the dangling O atoms based on their local structures. The dangling O atoms have either a D-NbO_3 or D-NbO_4 environment, as shown in Fig. 4 of the main text, where "D" represents the dangling O atom. These D-NbO_3 and D-NbO_4 patterns closely resemble the two locally stable TLS states, A and B [Fig. 2(a)], but with different Nb−O bond lengths. Hence, we treat them as effectively strained A or B states, whose TLSs are already known. Given that the local strains are anisotropic and bond-dependent, we define a TLS strain coupling coefficient, γ_i, for each Nb−O bond in the A and B states separately, written as

$$\gamma_i = \frac{1}{2}\frac{\partial \Delta}{\partial \varepsilon_i}. \tag{F1}$$

Here, i is the index of Nb−O bonds in the A or B states, sorted by bond lengths in descending order, Δ is the asymmetry energy of the corresponding TLS, and ε_i is the effective local strain on the ith bond, defined as the ratio of bond length changes. To determine γ_i, we impose a series of strains on the A and B states of TLS-I and TLS-II, and fit γ_i using the equation

$$\Delta = E_0 + \sum_{i=1,N} 2\gamma_i \varepsilon_i, \tag{F2}$$

where E_0 is the asymmetry energy without strains, and $N = 3$ (4) for D-NbO_3 (D-NbO_4). The values of E_0 and γ_i obtained through a least-squares fit are listed in Table III.

TABLE III. E_0 and TLS strain coupling coefficient γ_i for each bond of the locally stable states (A, B) of TLS-I and TLS-II, obtained through a least-squares fit.

	E_0 (meV)	γ_1 (eV)	γ_2 (eV)	γ_3 (eV)	γ_4 (eV)
TLS-I (A)	81	0.556	−3.418	−0.709	—
TLS-I (B)	81	0.204	−1.697	−2.645	0.889
TLS-II (A)	−21	−0.509	3.732	1.969	—
TLS-II (B)	−21	4.019	−1.774	1.138	—

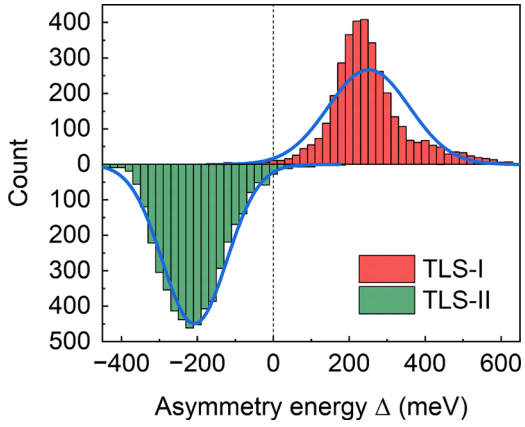

FIG. 13. Estimated distribution of the asymmetry energy Δ for TLS-I and TLS-II on surfaces of ten approximately 100 × 100 Å^2 amorphous Nb_2O_5 slabs. The blue lines represent Gaussian fits.

We then use Eq. (F2) to estimate the asymmetry energy Δ of the TLSs for all the dangling O atoms on amorphous Nb_2O_5 surfaces. To minimize errors, we perform statistical analyses on ten different amorphous surfaces. Each surface has a size of approximately 100×100 Å^2 and is generated with a cooling rate of 7.5 K/ps. The results are illustrated in Fig. 13, where both TLS-I and TLS-II exhibit Gaussian distributions with a considerable tail near the $\Delta = 0$ region. Note that this does not imply that they follow a Gaussian distribution in real systems, as for large $|\Delta|$ values (typically greater than 100 meV), one of the two locally stable states can be unstable, so only the regions near $\Delta = 0$ are meaningful. In a small energy region of -10 to 10 meV (4836 GHz), we observe 11 and 27 TLSs for TLS-I and -II, respectively. Since we consider both the top and bottom surfaces of ten approximately 100×100 Å^2 slabs, the total surface area amounts to 0.002 μm^2. Ultimately, we arrive at a TLS density $\sigma \approx 3.9/(\text{GHz}\,\mu\text{m}^2)$.

[1] J. Q. You and F. Nori, Superconducting circuits and quantum information, Phys. Today **58**, 42 (2005).

[2] J. Clarke and F. K. Wilhelm, Superconducting quantum bits, Nature **453**, 1031 (2008).

[3] M. Kjaergaard, M. E. Schwartz, J. Braumüller, P. Krantz, J. I.-J. Wang, S. Gustavsson, and W. D. Oliver, Superconducting qubits: Current state of play, Annu. Rev. Condens. Matter Phys. **11**, 369 (2020).

[4] I. Siddiqi, Engineering high-coherence superconducting qubits, Nat. Rev. Mater. **6**, 875 (2021).

[5] J. M. Martinis, K. B. Cooper, R. McDermott, M. Steffen, M. Ansmann, K. D. Osborn, K. Cicak, S. Oh, D. P. Pappas, R. W. Simmonds, and C. C. Yu, Decoherence in Josephson qubits from dielectric loss, Phys. Rev. Lett. **95**, 210503 (2005).

[6] C. Müller, J. H. Cole, and J. Lisenfeld, Towards understanding two-level-systems in amorphous solids: Insights from quantum circuits, Rep. Prog. Phys. **82**, 124501 (2019).

[7] P. W. Anderson, B. I. Halperin, and C. M. Varma, Anomalous low-temperature thermal properties of glasses and spin glasses, Philos. Mag. **25**, 1 (1972).

[8] W. A. Phillips, Tunneling states in amorphous solids, J. Low Temp. Phys. **7**, 351 (1972).

[9] A. M. Holder, K. D. Osborn, C. J. Lobb, and C. B. Musgrave, Bulk and surface tunneling hydrogen defects in alumina, Phys. Rev. Lett. **111**, 065901 (2013).

[10] L. Gordon, H. Abu-Farsakh, A. Janotti, and C. G. Van de Walle, Hydrogen bonds in Al_2O_3 as dissipative two-level systems in superconducting qubits, Sci. Rep. **4**, 7590 (2014).

[11] A. P. Paz, I. V. Lebedeva, I. V. Tokatly, and A. Rubio, Identification of structural motifs as tunneling two-level systems in amorphous alumina at low temperatures, Phys. Rev. B **90**, 224202 (2014).

[12] K. Agarwal, I. Martin, M. D. Lukin, and E. Demler, Polaronic model of two-level systems in amorphous solids, Phys. Rev. B **87**, 144201 (2013).

[13] D. Lee, J. L. DuBois, and V. Lordi, Identification of the local sources of paramagnetic noise in superconducting qubit devices fabricated on α-Al_2O_3 substrates using density-functional calculations, Phys. Rev. Lett. **112**, 017001 (2014).

[14] S. E. de Graaf, L. Faoro, L. B. Ioffe, S. Mahashabde, J. J. Burnett, T. Lindström, S. E. Kubatkin, A. V. Danilov, and A. Y. Tzalenchuk, Two-level systems in superconducting quantum devices due to trapped quasiparticles, Sci. Adv. **6**, eabc5055 (2020).

[15] Z.-H. Zhang, K. Godeneli, J. He, M. Odeh, H. Zhou, S. Meesala, and A. Sipahigil, Acceptor-induced bulk dielectric loss in superconducting circuits on silicon, Phys. Rev. X **14**, 041022 (2024).

[16] M. Constantin, C. C. Yu, and J. M. Martinis, Saturation of two-level systems and charge noise in Josephson junction qubits, Phys. Rev. B **79**, 094520 (2009).

[17] M. Constantin and C. C. Yu, Microscopic model of critical current noise in Josephson junctions, Phys. Rev. Lett. **99**, 207001 (2007).

[18] J. Verjauw, A. Potočnik, M. Mongillo, R. Acharya, F. Mohiyaddin, G. Simion, A. Pacco, T. Ivanov, D. Wan, A. Vanleenhove, and L. Souriau, Investigation of microwave loss induced by oxide regrowth in high-Q niobium resonators, Phys. Rev. Appl. **16**, 014018 (2021).

[19] A. Premkumar, C. Weiland, S. Hwang, B. Jäck, A. P. Place, I. Waluyo, A. Hunt, V. Bisogni, J. Pelliciari, A. Barbour, and M. S. Miller, Microscopic relaxation channels in materials for superconducting qubits, Commun. Mater. **2**, 72 (2021).

[20] A. A. Murthy, P. Masih Das, S. M. Ribet, C. Kopas, J. Lee, M. J. Reagor, L. Zhou, M. J. Kramer, M. C. Hersam, M. Checchin, and A. Grassellino, Developing a chemical and structural understanding of the surface oxide in a niobium superconducting qubit, ACS Nano **16**, 17257 (2022).

[21] M. V. P. Altoé, A. Banerjee, C. Berk, A. Hajr, A. Schwartzberg, C. Song, M. Alghadeer, S. Aloni, M. J. Elowson, J. M. Kreikebaum, and E. K. Wong, Localization and mitigation of loss in niobium superconducting circuits, PRX Quantum **3**, 020312 (2022).

[22] K. Zheng, D. Kowsari, N. J. Thobaben, X. Du, X. Song, S. Ran, E. A. Henriksen, D. S. Wisbey, and K. W. Murch, Nitrogen plasma passivated niobium resonators for superconducting quantum circuits, Appl. Phys. Lett. **120**, 102601 (2022).

[23] J. Verjauw, R. Acharya, J. Van Damme, T. Ivanov, D. P. Lozano, F. A. Mohiyaddin, D. Wan, J. Jussot, A. M. Vadiraj, M. Mongillo, and M. Heyns, Path toward manufacturable superconducting qubits with relaxation times exceeding 0.1 ms, Npj Quantum Inf. **8**, 93 (2022).

[24] M. Bal, A. A. Murthy, S. Zhu, F. Crisa, X. You, Z. Huang, T. Roy, J. Lee, D. V. Zanten, R. Pilipenko, and I. Nekrashevich, Systematic improvements in transmon qubit coherence enabled by niobium surface encapsulation, Npj Quantum Inf. **10**, 43 (2024).

[25] A. P. M. Place, L. V. Rodgers, P. Mundada, B. M. Smitham, M. Fitzpatrick, Z. Leng, A. Premkumar, J. Bryon, A. Vrajitoarea, S. Sussman, and G. Cheng, New material platform for superconducting transmon qubits with coherence

times exceeding 0.3 milliseconds, Nat. Commun. **12**, 1779 (2021).
[26] C. Wang, X. Li, H. Xu, Z. Li, J. Wang, Z. Yang, Z. Mi, X. Liang, T. Su, C. Yang, and G. Wang, Towards practical quantum computers: Transmon qubit with a lifetime approaching 0.5 milliseconds, Npj Quantum Inf. **8**, 3 (2022).
[27] M. Grundner and J. Halbritter, On the natural Nb_2O_5 growth on Nb at room temperature, Surf. Sci. **136**, 144 (1984).
[28] A. Bilmes, A. Megrant, P. Klimov, G. Weiss, J. M. Martinis, A. V. Ustinov, and J. Lisenfeld, Resolving the positions of defects in superconducting quantum bits, Sci. Rep. **10**, 3090 (2020).
[29] A. Bilmes, S. Volosheniuk, A. V. Ustinov, and J. Lisenfeld, Probing defect densities at the edges and inside Josephson junctions of superconducting qubits, Npj Quantum Inf. **8**, 24 (2022).
[30] P. E. Blöchl, Projector augmented-wave method, Phys. Rev. B **50**, 17953 (1994).
[31] G. Kresse and J. Furthmüller, Efficient iterative schemes for ab initio total-energy calculations using a plane-wave basis set, Phys. Rev. B **54**, 11169 (1996).
[32] G. Kresse and J. Hafner, Ab initio molecular-dynamics simulation of the liquid-metal–amorphous-semiconductor transition in germanium, Phys. Rev. B **49**, 14251 (1994).
[33] J. P. Perdew, K. Burke, and M. Ernzerhof, Generalized gradient approximation made simple, Phys. Rev. Lett. **77**, 3865 (1996).
[34] J. P. Perdew, K. Burke, and Y. Wang, Generalized gradient approximation for the exchange-correlation hole of a many-electron system, Phys. Rev. B **54**, 16533 (1996).
[35] G. Henkelman, B. P. Uberuaga, and H. Jónsson, A climbing image nudged elastic band method for finding saddle points and minimum energy paths, J. Chem. Phys. **113**, 9901 (2000).
[36] S. Grimme, J. Antony, S. Ehrlich, and H. Krieg, A consistent and accurate ab initio parametrization of density functional dispersion correction (DFT-D) for the 94 elements H-Pu, J. Chem. Phys. **132**, 154104 (2010).
[37] S. Grimme, S. Ehrlich, and L. Goerigk, Effect of the damping function in dispersion corrected density functional theory, J. Comput. Chem. **32**, 1456 (2011).
[38] K. Momma and F. Izumi, VESTA 3 for three-dimensional visualization of crystal, volumetric and morphology data, J. Appl. Crystallogr. **44**, 1272 (2011).
[39] R. Jinnouchi, J. Lahnsteiner, F. Karsai, G. Kresse, and M. Bokdam, Phase transitions of hybrid perovskites simulated by machine-learning force fields trained on the fly with Bayesian inference, Phys. Rev. Lett. **122**, 225701 (2019).
[40] R. Jinnouchi, F. Karsai, and G. Kresse, On-the-fly machine learning force field generation: Application to melting points, Phys. Rev. B **100**, 014105 (2019).
[41] R. Jinnouchi, F. Karsai, C. Verdi, R. Asahi, and G. Kresse, Descriptors representing two- and three-body atomic distributions and their effects on the accuracy of machine-learned inter-atomic potentials, J. Chem. Phys. **152**, 234102 (2020).
[42] J. Du and A. N. Cormack, *Atomistic Simulations of Glasses: Fundamentals and Applications* (John Wiley & Sons, Inc., Hoboken, New Jersey, 2022).
[43] J. K. Christie and A. Tilocca, Short-range structure of yttrium alumino-silicate glass for cancer radiotherapy: Car–Parrinello molecular dynamics simulations, Adv. Eng. Mater. **12**, B326 (2010).
[44] A. Tilocca, Structure and dynamics of bioactive phosphosilicate glasses and melts from ab initio molecular dynamics simulations, Phys. Rev. B **76**, 224202 (2007).
[45] J. Du and L. R. Corrales, Structure, dynamics, and electronic properties of lithium disilicate melt and glass, J. Chem. Phys. **125**, 114702 (2006).
[46] H. Wang, C. Shi, J. Hu, S. Han, C. C. Yu, and R. Q. Wu, Candidate source of flux noise in SQUIDs: Adsorbed oxygen molecules, Phys. Rev. Lett. **115**, 077002 (2015).
[47] Z. Wang, H. Wang, C. C. Yu, and R. Q. Wu, Hydrogen as a source of flux noise in SQUIDs, Phys. Rev. B **98**, 020403 (2018).
[48] T. S. Ercit, Refinement of the structure of ζ-Nb_2O_5 and its relationship to the rutile and thoreaulite structures, Mineral. Petrol. **43**, 217 (1991).
[49] I. P. Zibrov, V. P. Filonenko, M. Sundberg, and P.-E. Werner, Structures and phase transitions of B-Ta_2O_5 and Z-Ta_2O_5: Two high-pressure forms of Ta_2O_5, Acta. Crystallogr. B **56**, 659 (2000).
[50] H. M. Carruzzo, A. Bilmes, J. Lisenfeld, Z. Yu, B. Wang, Z. Wan, J. R. Schmidt, and C. C. Yu, Distribution of two-level system couplings to strain and electric fields in glasses at low temperatures, Phys. Rev. B **104**, 134203 (2021).
[51] G. J. Grabovskij, T. Peichl, J. Lisenfeld, G. Weiss, and A. V. Ustinov, Strain tuning of individual atomic tunneling systems detected by a superconducting qubit, Science **338**, 232 (2012).
[52] H. M. Carruzzo and C. C. Yu, Why phonon scattering in glasses is universally small at low temperature, Phys. Rev. Lett. **124**, 075902 (2020).
[53] W. Tang, E. Sanville, and G. Henkelman, A grid-based Bader analysis algorithm without lattice bias, J. Phys.: Condens. Matter **21**, 084204 (2009).
[54] B. Sarabi, A. N. Ramanayaka, A. L. Burin, F. C. Wellstood, and K. D. Osborn, Projected dipole moments of individual two-level defects extracted using circuit quantum electrodynamics, Phys. Rev. Lett. **116**, 167002 (2016).
[55] D. J. Griffiths and D. F. Schroeter, *Introduction to Quantum Mechanics* (Cambridge University Press, Cambridge, UK, 2018).
[56] C. Enss and S. Hunklinger, *Low-Temperature Physics* (Springer-Verlag, Berlin, 2005).
[57] J. Lisenfeld, A. Bilmes, A. Megrant, R. Barends, J. Kelly, P. Klimov, G. Weiss, and J. M. Martinis, Electric field spectroscopy of material defects in transmon qubits, Npj Quantum Inf. **5**, 105 (2019).
[58] M. Von Schickfus and S. Hunklinger, Saturation of the dielectric absorption of vitreous silica at low temperatures, Phys. Lett. **64A**, 144 (1977).
[59] J. Lisenfeld, A. Bilmes, and A. V. Ustinov, Enhancing the coherence of superconducting quantum bits with electric fields, Npj Quantum Inf. **9**, 8 (2023).
[60] C. Nico, T. Monteiro, and M. P. F. Graça, Niobium oxides and niobates physical properties: Review and prospects, Prog. Mater Sci. **80**, 1 (2016).

[61] C. Valencia-Balvín, S. Pérez-Walton, G. M. Dalpian, and J. M. Osorio-Guillén, First-principles equation of state and phase stability of niobium pentoxide, Comput. Mater. Sci. **81**, 133 (2014).

[62] M. B. Pinto, A. L. Soares, Jr, A. Mella Orellana, H. A. Duarte, and H. A. De Abreu, Structural, electronic, and thermodynamic properties of the T and B phases of niobia: First-principle calculations, J. Phys. Chem. A **121**, 2399 (2017).

[63] S. Pérez-Walton, C. Valencia-Balvín, A. C. M. Padilha, G. M. Dalpian, and J. M. Osorio-Guillén, A search for the ground state structure and the phase stability of tantalum pentoxide, J. Phys.: Condens. Matter **28**, 035801 (2016).

[64] D. D. Wagman, The NBS tables of chemical thermodynamic properties: Selected values for inorganic and C1 and C2 organic substances in SI units (American Chemical Society, Washington, 1982), J. Phys. Chem. Ref. Data **11**, Suppl. 2 (1982).

[65] M. B. Pinto, A. L. Soares, Jr, M. C. Quintão, H. A. Duarte, and H. A. De Abreu, Unveiling the structural and electronic properties of the B-Nb_2O_5 surfaces and their interaction with H_2O and H_2O_2, J. Phys. Chem. C **122**, 6618 (2018).